npj | 2D Materials and Applications

www.nature.com/npj2dmaterials

ARTICLE OPEN

Check for updates

Probing valley population imbalance in transition metal dichalcogenides via temperature-dependent second harmonic generation imaging

Leonidas Mouchliadis[1]✉, Sotiris Psilodimitrakopoulos[1], George Miltos Maragkakis[1,2], Ioanna Demeridou[1,2], George Kourmoulakis[1,3], Andreas Lemonis[1], George Kioseoglou[1,3] and Emmanuel Stratakis[1,2]✉

Degenerate minima in momentum space—valleys—provide an additional degree of freedom that can be used for information transport and storage. Notably, such minima naturally exist in the band structure of transition metal dichalcogenides (TMDs). When these atomically thin crystals interact with intense laser light, the second harmonic generated (SHG) field inherits special characteristics that reflect not only the broken inversion symmetry in real space but also the valley anisotropy in reciprocal space. The latter is present whenever there exists a valley population imbalance (VPI) between the two valleys and affects the polarization state of the detected SHG. In this work, it is shown that the temperature-induced change of the SHG intensity dependence on the excitation field polarization is a fingerprint of VPI in TMDs. In particular, pixel-by-pixel VPI mapping based on polarization-resolved raster-scanning imaging microscopy was performed inside a cryostat to generate the SHG contrast in the presence of VPI from every point of a TMD flake. The generated contrast is marked by rotation of the SHG intensity polar diagrams at low temperatures and is attributed to the VPI-induced SHG.

npj 2D Materials and Applications (2021)5:6 ; https://doi.org/10.1038/s41699-020-00183-z

INTRODUCTION

Conventional optoelectronics is based on the manipulation of electronic charge with light, for information transport, storage, and readout. In electronic systems with degenerate minima in their band structure—valleys—an additional degree of freedom that labels those minima, i.e., the valley index, can serve as the information carrier. Such a possibility has opened an alternative field of electronics, namely valleytronics, which enables the processing of additional information within the same physical space[1–3]. Specifically, the valley index can be mapped to a pseudospin that, similar to the response of a spin to magnetic fields, is affected by the Berry curvature of the bands[4,5].

In transition metal dichalcogenides (TMDs), the valley pseudospin is coupled to the electron spin[6] to give rise to selection rules that allow the excitation of carriers in specific valleys only when light of suitable helicity is used[7–9]. More specifically, the excitation and control of carriers is achieved by circularly polarized light that populates only one of the two valleys. Interestingly, the polarization is transferred to and subsequently measured in the emitted (one- and two-photon) photoluminescence (PL)[10–12]. Such measurements are used to indirectly probe the population imbalance in different valleys.

Several other phenomena, associated with the existence of valleys and related with time reversal symmetry, have been reported in atomically thin crystals with hexagonal structure and corresponding degenerate (but inequivalent) K and K′ valleys in the hexagonal Brillouin zone. For example, in the presence of external fields, the valley imbalance may generate valley currents that give rise to valley Hall conductivity[13,14]. In addition, when linearly polarized light is used for excitation, superpositions of excitons in different valleys are created and one can measure valley coherence[15,16]. Valley injection and transport may be used to create a valley filter, i.e., a means to populate a single valley and therefore induce valley polarization. Serial combination of two such filters acts as a valley valve that can be externally controlled[17,18]. Moreover, although intervalley scattering is suppressed in ideal crystals, there are recent reports of intervalley collective modes in the presence of unequal valley populations[19].

In all the aforementioned cases, the common underlying physical principle is the population imbalance between different valleys. This is reasonable considering that polarization and transport effects are associated with charge separation and local variations in the chemical potential, respectively. Hence, they directly reflect the crystal symmetries in both real and momentum space. In real space, the charge is locally accumulated around the atomic positions, whereas in momentum space, the carriers occupy states in the vicinity of high symmetry points within the hexagonal Brillouin zone. Interestingly, both polarization and transport effects can be examined by analyzing the second-order nonlinear optical response of atomically thin crystals.

Recently, SHG spectroscopy has been highly appreciated as a powerful tool to study two-dimensional (2D) TMDs[20–27]. Owing to the vanishing thickness of these thin crystals, phase-matching conditions are readily satisfied and thus the second-order nonlinear susceptibility, $\chi^{(2)}$, is large[28]. Under the D_{3h} point group symmetry of TMD crystals, the $\chi^{(2)}$ tensor exhibits non-vanishing elements for odd-layer TMDs in 2H configuration and for arbitrary-layered in 3R stacking geometry[28]. These elements are not independent but are inter-related through: $\chi^{(2)}_{xxx} = -\chi^{(2)}_{xyy} = -\chi^{(2)}_{yyx} = -\chi^{(2)}_{yxy} = \chi^{(2)}_{\mathrm{int}}$ where x denotes the crystal mirror symmetry axis, i.e., the armchair direction, y is the zig-zag direction and $\chi^{(2)}_{\mathrm{int}}$ is the nonzero element of the intrinsic second-order susceptibility tensor.

[1]Institute of Electronic Structure and Laser-Foundation for Research and Technology-Hellas, Heraklion 70013, Greece. [2]Physics Department, University of Crete, Heraklion 71003, Greece. [3]Department of Materials Science and Technology, University of Crete, Heraklion 71003, Greece. ✉email: mouhliad@physics.uoc.gr; stratak@iesl.forth.gr

Published in partnership with FCT NOVA with the support of E-MRS

npj nature partner journals

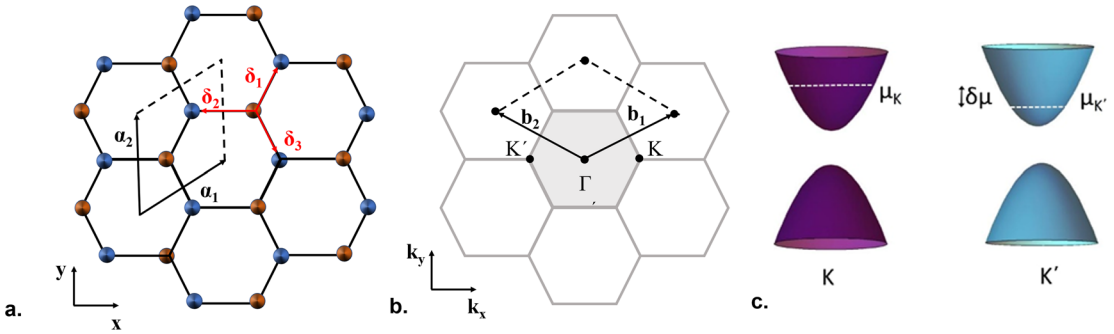

Fig. 1 Crystal structure, Brillouin zone, and dispersion of monolayer transition metal dichalcogenides. a Top view of monolayer TMD honeycomb lattice with transition metal atoms in red and chalcogen atoms in blue. The lattice vectors a_1 and a_2 and first-neighbor vectors δ_1, δ_2, and δ_3 are also shown. The region bounded by dashed lines corresponds to the primitive cell. **b** First Billouin zone (shaded) of monolayer TMD showing the high symmetry points Γ, K, and K′. The reciprocal lattice vectors b_1 and b_2 are also depicted. **c** Schematic of monolayer TMD dispersion. The paraboloids represent valence and conduction bands at K (purple) and K′ (cyan) points. The white dashed lines indicate the chemical potential at different valleys for the case of population imbalance.

In addition, both SHG intensity and polarization have been found to reveal information about the main crystallographic axis[20,21,25,26], grain boundaries[29,30], stacking sequence, twist angle[24,27], number of layers, and crystal homogeneity[26]. Indeed, the ability to control the polarization state of the SHG signal enables the extraction of additional information from a single measurement, since the second-order response is determined by a third rank susceptibility tensor[31]; therefore, measurements at higher order of response enable access to a larger number of independent quantities of a system[32,33].

Recent theoretical studies suggest that the second-order optical response is also a useful tool to probe the electronic configuration of 2D crystals[32,34,35]. This is possible due to the symmetry characterizing the hexagonal Brillouin zone in momentum space. Similarly to the alternating atoms at the corners of the hexagon in real space, characterized by the D_{3h} symmetry of the trigonal prismatic structure with Bernal stacking (Fig. 1a), in momentum space the alternating K and K′ points also result in D_{3h} symmetry, reflecting the trigonal warping of electrons in the vicinity of high symmetry points (Fig. 1b)[36]. Besides, the conduction and valence band states at the corners of the hexagonal Brillouin zone are formed by hybridization of the transition metal *d*-orbitals with the chalcogen *p*-orbitals and therefore are strongly localized in the metal atom plane[37–39]. A direct consequence of this effect is the possibility for such crystals to produce valley-induced SHG, additionally to the intrinsic second-order response. As a result, in the presence of population imbalance between the two valleys, additional elements in the second-order nonlinear optical susceptibility tensor become nonzero[32,34,35,40]. Therefore, we have: $\chi^{(2)}_{yyy} = -\chi^{(2)}_{yxx} = -\chi^{(2)}_{xxy} = -\chi^{(2)}_{xyx} = \chi^{(2)}_{\mathrm{vpi}}$, where $\chi^{(2)}_{\mathrm{vpi}}$ is the nonzero element of the valley population imbalance (VPI)-induced second-order susceptibility tensor.

VPI can be either induced[10,40] or emerge spontaneously[41] and depending on the way it is created, it reflects different aspects of the electronic system. For instance, when circularly polarized light is used for excitation, only one of the two valleys is populated and the spin-valley polarization is transferred to the detected one- or two-photon PL[15]. In contrast, for linearly polarized light, a superposition of excitons in the K and K′ valleys is created and one can measure valley coherence[16]. Even at equilibrium, i.e., valley population balance, there is a small, but finite probability that an electron will be transferred to the adjacent valley, while at the same time flipping its spin, thus perturbing the balance. In this last case, access to the degree of VPI would reveal information about the intrinsic valley relaxation time[41].

In this work, we take advantage of the temperature dependence of polarization-resolved SHG (PSHG) to account for the VPI in atomically thin TMDs. Notably, since the VPI defines the difference between the valley populations, $\delta n = n_K - n_{K'}$, it also reflects the chemical potential difference, $\delta\mu$, between the two valleys (Fig. 1c). Hence, in the presence of imbalance, the additional valley-induced contribution to the SHG that is intrinsically generated by the TMD crystal, can be estimated as

$$I^{\mathrm{VPI}}_{\mathrm{SHG}} \sim \delta n^2 \sim \delta\mu^2 \quad (1)$$

with the corresponding contribution to the second-order nonlinear susceptibility being proportional to the chemical potential difference, i.e., $\chi^{(2)}_{\mathrm{vpi}} \sim \delta\mu$[34,35,41]. Accordingly, local variations in the chemical potential affect the SHG induced by the VPI and thus can be probed by nonlinear optical experiments[40]. More importantly, and in contrast to the intrinsic nonlinear optical response of 2D TMDs, the valley-induced SHG is sensitive to temperature variations. Based on this, we here vary the temperature of a 2D TMD crystal and the corresponding changes in the SHG intensity are used to probe the intervalley chemical potential difference and therefore the VPI.

We consider an electromagnetic field that is normally incident to a 2D TMD sample with polarization parallel to the sample plane, at an angle φ (Fig. 2a); the crystal armchair direction is oriented at an angle θ. Here we implement the experiment proposed by Hipolito and Pereira[32], in which a quarter-wave plate is placed before the sample with its fast axis at an angle α. Using a half-wave plate we control the orientation φ of the fundamental linear polarization, while a linear polarizer placed before the detector at an angle ζ, selects suitable SHG components. All angles are measured with respect to the laboratory *X*-axis. The linear polarization of the excitation changes to elliptical as the beam passes through the quarter-wave plate whose axis has an offset of 5° with respect to the polarization axis. Such a configuration provides the means for an asymmetric population of the two valleys[40]. An accurate description of the polarization state of the fundamental field incident to the sample and the SHG field emerging from the 2D crystal entails the use of the Jones formalism and is presented in detail in the Supplementary Eqs. (1)–(10).

PSHG imaging was performed in 78–300 K temperature range using a fs laser-scanning microscope coupled with a liquid nitrogen cryogenic system (Fig. 2b; see also "Methods"). The infrared laser beam is guided into an inverted microscope, while its polarization is controlled by properly rotating half- and quarter-wave plates. A pair of galvanometric mirrors enables raster-scanning of the sample, which is placed inside a continuous flow cryostat. The SHG signal from the sample passes through a rotating linear polarizer and is collected in reflection geometry. Different rotation speeds of the optical elements allows control over the angles φ, α and ζ. The armchair direction θ can be determined with the same experimental setup[26].

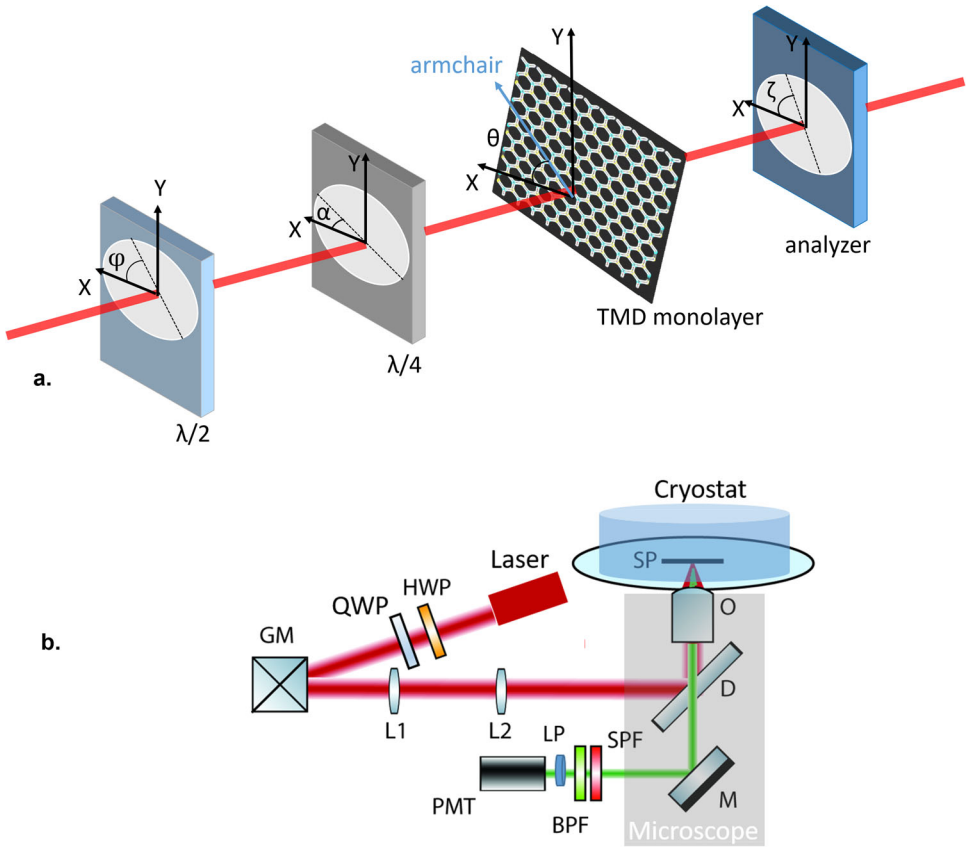

Fig. 2 Experimental configuration and setup. a Cartoon of the experimental configuration. The definition of the angles φ, α, θ, and ζ is shown, in terms of the laboratory coordinate system (X, Y black axes) and the fast axes (dashed lines) of the optical elements. **b** Sketch of the experimental setup. An infrared fs laser excites a 2D TMD held inside the cryostat. The SHG signal emerging from the sample is directed to the detector in reflection geometry. HWP half-wave plate, QWP quarter-wave plate, GM galvanometric mirrors, L1, L2 lenses, D dichroic mirror, O objective lens, SP sample plane, M mirror, SPF short-pass filter, BPF bandpass filter, LP linear polarizer, PMT photomultiplier tube.

For the PL measurements, a micro-PL setup was used to collect PL in a backscattering geometry (see also "Methods"). Emitted light was dispersed by a single monochromator equipped with a multichannel CCD detector. Following the excitation, the emitted PL spectra were analyzed as σ^+ and σ^- using a combination of quarter-wave plate and linear polarizer placed in front of the spectrometer entrance slit. A cryogenic system was coupled with the optical setups to perform temperature-dependent second harmonic and spin-valley polarization measurements in a range of temperatures from 78 up to 300 K.

Application of nonlinear optics for a crystal with D_{3h} symmetry in the presence of VPI yields the SHG field emerging from the crystal as[42,43]

$$\begin{pmatrix} P_x^{2\omega} \\ P_y^{2\omega} \end{pmatrix} \sim \begin{pmatrix} \chi_{\mathrm{int}}^{(2)}\left(E_x^2 - E_y^2\right) - 2\chi_{\mathrm{vpi}}^{(2)}E_xE_y \\ -\chi_{\mathrm{vpi}}^{(2)}\left(E_x^2 - E_y^2\right) - 2\chi_{\mathrm{int}}^{(2)}E_xE_y \end{pmatrix}. \quad (2)$$

Here $\chi_{\mathrm{int}}^{(2)}$ and $\chi_{\mathrm{vpi}}^{(2)}$ correspond to the intrinsic and induced due to VPI contributions to the second-order response, respectively. This means that the SHG intensity reaching the detector depends on four angles, namely φ, θ, α, ζ, corresponding to the effects of excitation linear polarization, crystal orientation, quarter-wave plate, and analyzer, respectively (Fig. 2). In this case, the detected SHG intensity is given by

$$I_{2\omega} = A[\cos(2\alpha + \zeta - 3\theta) - \kappa\sin(2\alpha + \zeta - 3\theta)]^2 + [\kappa\cos(2\alpha + \zeta - 3\theta) + \sin(2\alpha + \zeta - 3\theta)]^2 \sin^2[2(\alpha - \varphi)], \quad (3)$$

where κ denotes the magnitude of VPI-induced to intrinsic susceptibility ratio

$$\kappa = \frac{|\chi_{\mathrm{vpi}}^{(2)}|}{|\chi_{\mathrm{int}}^{(2)}|} \quad (4)$$

and A is a multiplication factor that depends on the amplitude of the field and the intrinsic second-order susceptibility. The ratio κ can be extracted upon fitting the experimentally measured PSHG intensity with Eq. (3) and reflects the degree of VPI. In our experiment, the optical elements are controlled using motorized stages synchronized to rotate in phase giving rise to a six-petal pattern for the PSHG intensity (see also Fig. S6).

RESULTS AND DISCUSSION

Temperature-dependent imaging of VPI

WS_2 samples were prepared with mechanical exfoliation and characterized using Raman mapping (see "Methods"). Figure 3a shows an optical image of the sample where the monolayer (1L) region is indicated. In order to quantify the VPI, we fit the experimentally measured SHG intensity at each temperature with Eq. (3) to extract the dimensionless parameter κ. For 300 K, in particular, we assume that the valley-induced SHG is negligible ($\kappa = 0$) and use the same equation to determine the armchair orientation θ. As shown in Fig. 3b, c, the SHG intensity as well as the VPI mapping of WS_2 at 78 K appear to be relatively uniform across the sample area yielding a value of $\kappa = 0.1$. However, several points of the flake boundaries correspond to increased or decreased

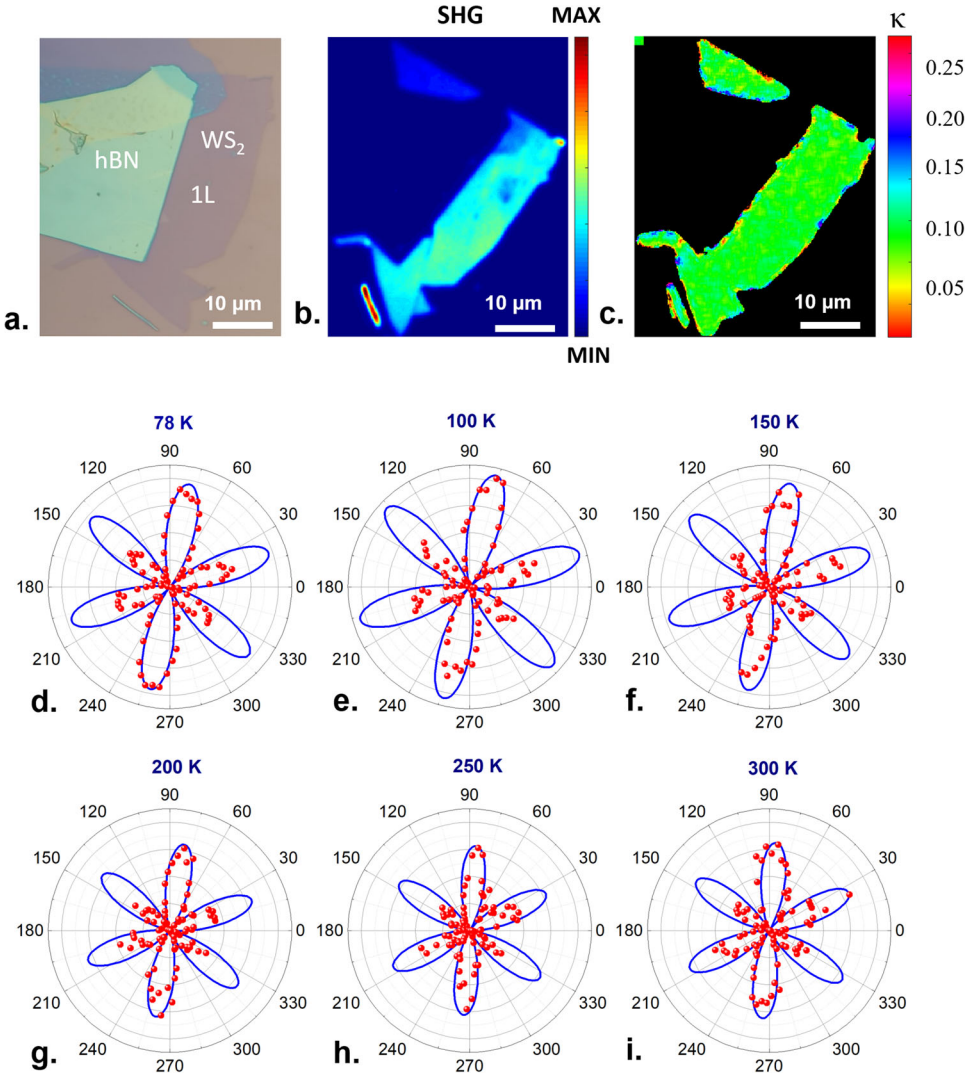

Fig. 3 Temperature-dependent imaging of valley population imbalance in monolayer WS_2. a Optical image of the WS_2 sample. **b** SHG intensity mapping of monolayer WS_2 at 78 K. **c** Imaging of VPI in terms of parameter κ, at 78 K. **d–i** PSHG intensity polar diagrams as a function of the incident field polarization angle, φ, for temperatures 78, 100, 150, 200, 250, and 300 K, respectively. The red spheres correspond to experimental data and the blue line is the fitting with Eq. (3).

κ values, most probably originating from local field effects that affect the electron distribution in the valleys, hence the VPI.

In Fig. 3d–i we present polar plots of the SHG emerging from the same monolayer region as a function of the excitation field polarization angle, for temperatures ranging from 78 to 300 K. The effect of low temperature is to preserve VPI by hindering the relaxation processes due to scarcity of phonons[44]; this effect is readily imprinted onto the PSHG patterns. As a consequence, as the temperature rises the PSHG intensity becomes progressively lower (see also Fig. 4), indicating the suppression of VPI.

The asymmetry in the size of the lobes in the polar diagrams stems from the well-known effect of polarization scrabbling due to the use of dichroic mirror in front of the microscope objective[45]. A forward detection geometry would produce polar diagrams with symmetric lobes. However, such a configuration was not possible in our case, since the experiments were performed inside a cryostat and the sample had to be placed on a non-transparent substrate. Thus, the asymmetry in the lobes, which is the same for all examined temperatures and pixels, is a known systematic error due to the use of dichroic mirror and affects only the quality of fitting and not our main observation, i.e., the rotation of the polar pattern with temperature. This is readily shown in the Supplementary Video where the polar diagrams taken from every pixel of a large image exhibit the same rotation with lowering temperature.

All polar diagrams presented in our work were taken from a single pixel from an image consisting of 500 × 500 pixels with pixel dwell time of ~1 μs. The experimental data (red spheres)—obtained from representative monolayer regions of interest—are fitted with Eq. (3) (blue line) and the theoretically predicted features of the polar patterns[32] are indeed identified: (a) increase in intensity at low temperatures where we expect larger values of population imbalance, (b) rotation of the low-temperature polar diagram—with respect to the ambient temperature one—as it can no longer be exclusively associated with the armchair direction. These features are summarized in Fig. 4a, where the fitted SHG polar diagrams for the minimum and maximum temperature are compared. The rotation of the polar pattern at low temperature originates from the additional elements in the second-order susceptibility tensor that have to be taken into account in the presence of VPI.

The monotonic decrease of the SHG with temperature (Fig. 4b) is reflected in the temperature dependence of κ-ratio (Fig. 4c). For comparison, we present in Fig. 4d the degree of spin-valley

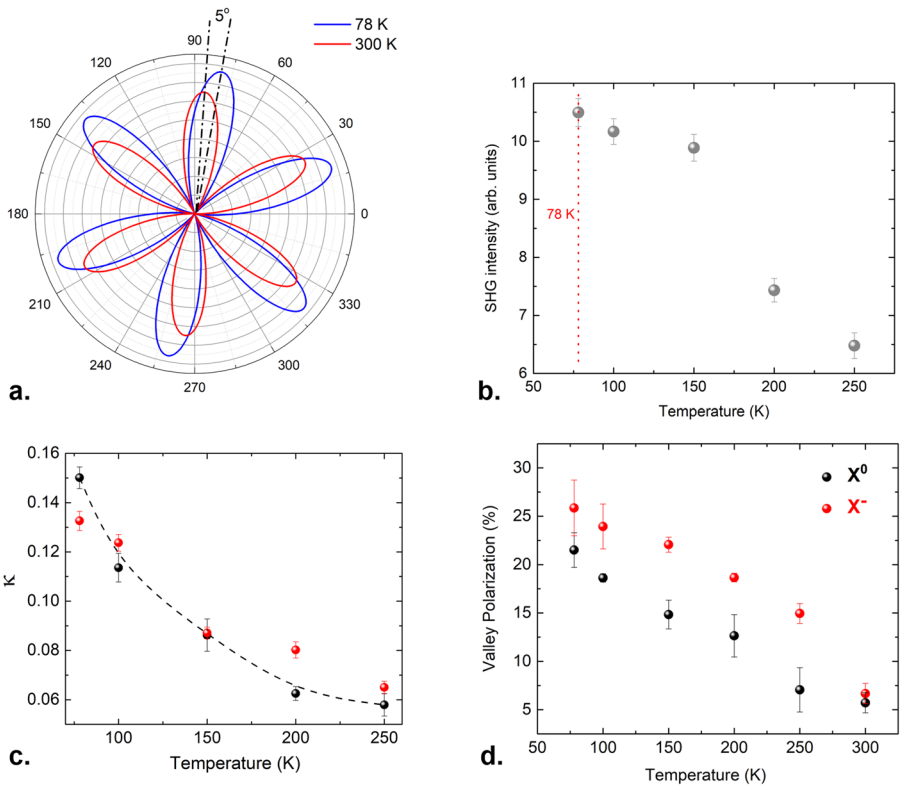

Fig. 4 Temperature dependence of second harmonic generation intensity, valley population imbalance and spin-valley polarization. **a** Comparison between the SHG polar diagrams fitted to the experimental data, for the highest (red) and lowest (blue) considered temperatures. With decreasing temperature, the SHG intensity increases due to the valley-induced contribution. A rotation of the polar diagram away from the main crystallographic axis is also reported. **b** Temperature dependence of the integrated SHG intensity. **c** Temperature dependence of the calculated parameter κ, for two regions of interest. **d** PL measurements of temperature-dependent spin-valley polarization for the neutral (black) and charged (red) exciton in the same sample.

polarization as a function of temperature for the neutral and charged excitons, obtained from PL measurements performed in the same sample (see also Supplementary Fig 2). It is evident that the degrees of VPI and spin-valley polarization both exhibit a monotonic reduction with temperature. We attribute both effects to the balancing of the populations in different valleys at elevated temperatures.

In order to further validate our method, we examined another flake of exfoliated WS_2, comprising monolayer, few-layer and bulk regions (Fig. 5a). The SHG intensity from the monolayer region at 78 K is higher than the multilayer one, as it is clearly shown in Fig. 5b. In contrast, the VPI, depicted in Fig. 5c in terms of the parameter κ, is higher in the few-layer region. This is actually expected, since there is an additional contribution to the valley-induced SHG from the extra layers. PL measurements also demonstrate a higher degree of valley polarization in the few-layer region compared to the monolayer one (Supplementary Fig. 5), further supporting the increased value of κ due to the additional layers[46,47]. Finally, we present polar diagrams of PSHG intensity at different temperatures for monolayer (Fig. 5d–f) and few-layer regions (Fig. 5g–i). The experimental data (red spheres) —obtained from representative regions of interest—are fitted with Eq. (3) (blue line) and the fingerprints of VPI are again identified: Similar to the single layer case presented previously, as the temperature rises from 78 to 200 K, the maximum SHG intensity decreases and the polar diagram is rotated.

The PSHG method for imaging VPI can be applied simultaneously to different atomically thin crystals. For instance, within the same field of view one can image the VPI of adjacent crystalline areas consisting of different 2D TMD flakes as demonstrated in Fig. 6, showing the WS_2 flake presented above together with a WSe_2 monolayer in the same field of view (Fig. 6a). Juxtaposing the SHG from the WS_2 and WSe_2 monolayers, we observe that the latter exhibits increased intensity at the excitation wavelength we have used (1030 nm) (Fig. 6b). On the contrary, the VPI imaging (Fig. 6c) and histogram (Fig. 6d) in terms of the parameter κ reveal that WS_2 is found to have slightly higher κ values. Notably, apart from a quantification of the VPI, the method presented here provides an optical way to determine the monolayer nature of a TMD crystal and discriminate regions consisting of different TMDs.

In conclusion, we have presented an all optical nonlinear method based on PSHG that enables the quantification and imaging of VPI in 2D TMDs. The demonstrated approach relies in analyzing the temperature-dependent changes in the PSHG intensity pattern as a function of the incident polarization angle. Fitting of the experimental data with a nonlinear optics model reveals the susceptibility ratio κ between the intrinsic and valley-induced second-order response of the TMD crystal. The PSHG-based method is suitable for large crystalline areas containing various 2D TMDs either adjacent or in stacked geometry.

Considering that VPI is the fundamental physical principle behind a plethora of phenomena, including valley polarization, valley coherence, valley Hall conductivity and valley filtering, its quantification is of great importance for advances in the field of valleytronics. We envisage the work presented herein as a significant step towards this effort.

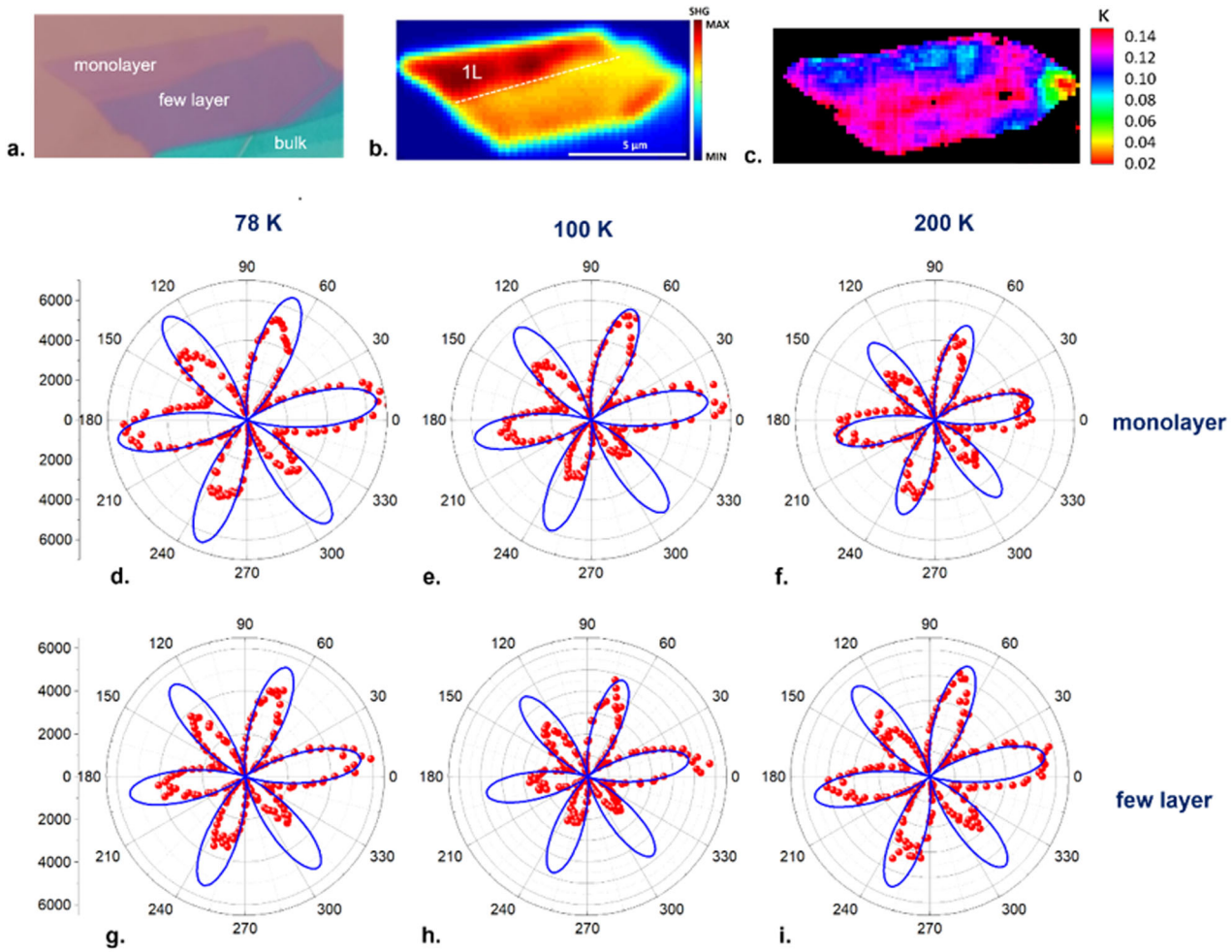

Fig. 5 Valley population imbalance imaging for monolayer and few-layer WS_2. a Optical image of a WS_2 flake consisting of monolayer, few-layer and bulk regions. **b** SHG intensity mapping of the WS_2 flake at 78 K. **c** Imaging of VPI in terms of the dimensionless parameter κ at 78 K. **d–f** Polar diagrams of SHG intensity with varying angle φ of incident field polarization at 78, 100, and 200 K for monolayer and **g–i** few-layer regions. Red spheres correspond to experimental data and the blue line to the fitting with Eq. (3).

METHODS

Sample preparation

Polydimethylsiloxane films (PDMS) were fabricated from 10:1 mixing ratio of SYLGARD 182 Silicone Elastomer Kit with heat cure at 80 °C for 2 h. WS_2 and WSe_2 bulk crystals, purchased from HQ Graphene, were mechanically exfoliated on the PDMS films placed on microscope glass slides[48,49]. Monolayers of these crystals were realized under an optical microscope and characterized with Raman spectroscopy. Then, the glass slides with PDMS films containing the monolayers were mounted on a XYZ micromechanical stage, placed under a coaxially illuminated microscope. The WS_2 and WSe_2 monolayers were transferred on Si/SiO_2 (285 nm) substrate using viscoelastic stamping[50].

Optical spectroscopy measurements

We used a micro-PL setup with a ×50 objective and appropriate filters and incorporated a liquid nitrogen-cooled cryostat to collect PL in a backscattering geometry. Emitted light was dispersed by a single monochromator equipped with a multichannel CCD detector. For optical spectroscopy measurements we used a combined μ-PL setup. A Mitutoyo ×50 lens (NA: 0.42, $f = 200$ mm) was used to focus the excitation beam onto the sample, down to ~1 μm size. The samples were held inside a continuous flow cryostat (ST500, Jannis, USA); their exact position was controlled by a XYZ mechanical translation stage (PT3, Thorlabs, USA) and the excitation procedure was continuously monitored via a CCD optical setup. Following the excitation, the emitted PL signal passes through a long pass filter to eliminate the emission of the laser. The PL spectra were analyzed as σ^+ and σ^- using a combination of a quarter-wave plate (liquid crystal) and a linear polarizer placed in front of the spectrometer entrance slit.

Temperature-dependent measurements

A cryogenic system has been coupled with the optical setup to perform temperature-dependent second harmonic and spin-valley polarization measurements in a range of temperatures from 78 up to 300 K. The cryogenic system consists of the liquid nitrogen-cooled cryostat (ST500, Janis, USA), the transfer line (Standard Flexible Transfer Line, Janis, USA), a liquid nitrogen 20lt storage dewar (Janis, USA), a temperature controller, a mechanical pump, and a turbo pump.

Raman characterization

Raman characterization was employed to verify the monolayer character of the samples. A Nicolet Almega XR μRaman analysis system (Thermo Scientific Instruments, Waltham MA USA) was used. The excitation wavelength was 473 nm and characterization was performed under ambient conditions. A set of data was collected from several regions across the WS_2 and WSe_2 monolayer areas (Supplementary Figs. 3a and 4a). Exposure time, laser intensity, and number of acquisitions were kept constant for all experiments. There is a variation in the intensity of different areas in the monolayer (Supplementary Figs 3b and 4b). For WS_2, analysis of the peak positions of the two most prominent Raman vibrational modes

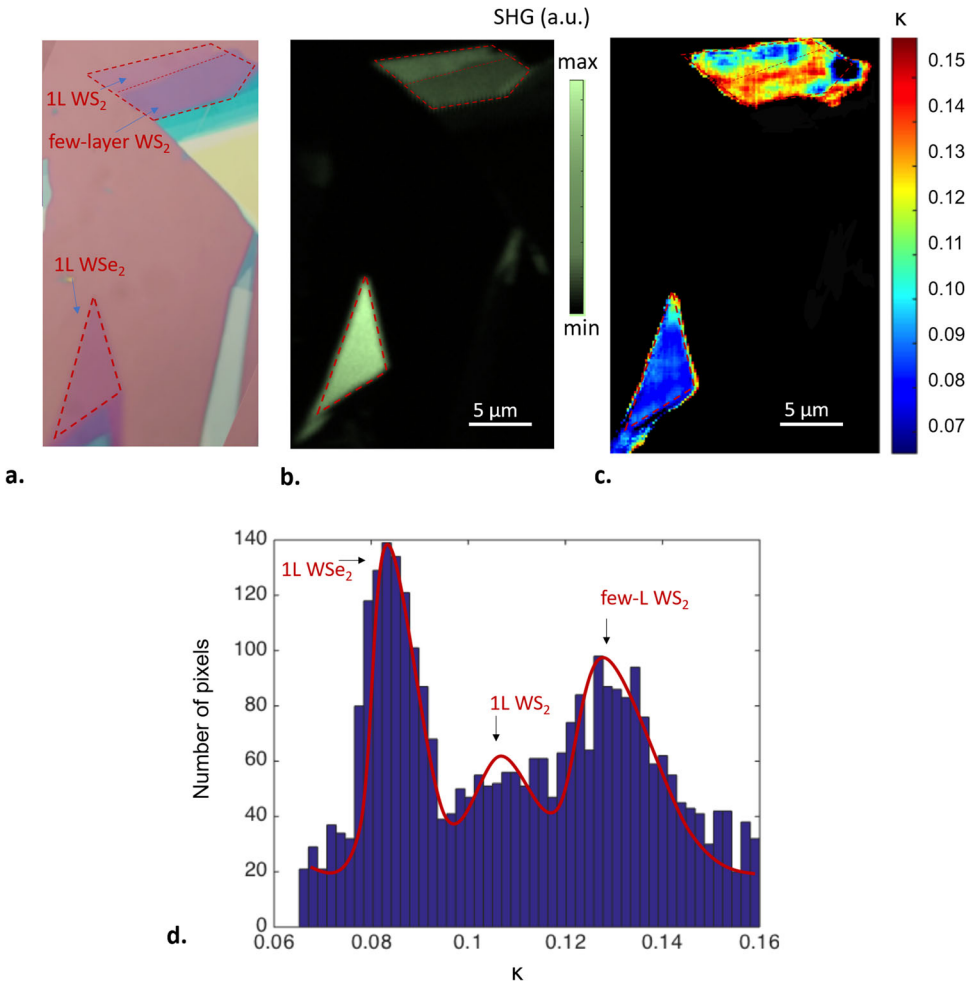

Fig. 6 Comparison of valley population imbalance between atomically thin WS_2 and WSe_2. **a** Optical image of a large area comprising monolayer and few-layer WS_2 as well as monolayer WSe_2. The corresponding areas are encircled by the red dashed lines. **b** SHG intensity imaging at 78 K. **c** VPI imaging and **d** histogram in terms of the dimensionless parameter κ at 78 K.

A_1' (out of plane) and E′ (in plane) is an indicator of the monolayer character of the sample. In all cases, the difference was ranging from 59 to 61 cm^{-1}, which confirms the existence of the monolayer in all studied areas (Supplementary Fig. 3c). Similarly for WSe_2, E′ (in plane) vibrational mode is positioned around 249 cm^{-1} and A_1 (out of plane) vibrational mode is at 260 cm^{-1} (Supplementary Fig. 4c). Raman mapping revealed a difference of 11 cm^{-1}, which also indicates monolayer thickness for WSe_2. Finally, Raman characterization of the WS_2 sample comprising monolayer, few-layer, and bulk areas (Supplementary Fig. 5a) was performed at liquid nitrogen conditions, with an excitation energy of 543 nm. The corresponding Raman spectra for the three areas (Supplementary Figs 5d–f) suggest that they comprise one, two to three, and above six layers, respectively.

Polarization-resolved second harmonic generation imaging

PSHG imaging was performed using an fs laser raster-scanning microscope coupled with a liquid nitrogen cryogenic system (ST500, Janis, USA) (Fig. 2b). The laser beam from a diode-pumped Yb:KGW fs oscillator (1030 nm, 70–90 fs, 76 MHz, Pharos-SP, Light Conversion, Lithuania) is guided into an inverted microscope (modified Axio Observer Z1, Carl Zeiss, Germany). In order to control the polarization of the fundamental field, we use two motorized rotation stages of high accuracy (0.1°) (M-060.DG, Physik Instrumente, Karlsruhe, Germany), holding a half-wave plate (QWPO-1030-10-2, CVI Laser, USA) and a quarter-wave plate (QWPO-1030-10-4, CVI Laser, USA). A pair of galvanometric mirrors (6215H, Cambridge Technology, Bedford, MA, USA) directs the beam into the microscope, enabling raster-scanning of the stationary sample placed inside a continuous flow cryostat (ST500, Janis, USA). Then, a pair of lenses forming a telescope suitably expands the beam to fill the back aperture of the microscope objective lens (×50, 0.55 NA, M Plan Apo, Mitutoyo, Japan). Given that the cryostat is not permeable, we collect the SHG in the backward (epi-) direction, with the same objective used for excitation and a short-pass dichroic mirror (DMSP805R, Thorlabs, USA) at the microscope turret box. The SHG signal is then filtered by suitable short-pass (FF01-680/SP, Semrock, Rochester, NY, USA) and narrow bandpass filters (FF01-514/3, Semrock, Rochester, NY, USA), to separate it from fundamental and absorption-induced radiation. Finally, SHG passes through a linear polarizer (LPVIS100-MP, ThorLabs, USA) placed on a third motorized rotation stage in front of the detector, which is based on a PMT module (H9305-04, Hamamatsu, Hamamatsu City, Japan). Coordination of PMT recordings with the galvanometric mirrors for the image formation, as well as the movements of all motors, is carried out using LabView (National Instruments, USA).

DATA AVAILABILITY

The data that support the findings of this study are available from the corresponding authors upon reasonable request.

Received: 17 June 2020; Accepted: 25 November 2020;
Published online: 04 January 2021

REFERENCES

1. Akinwande, D., Petrone, N. & Hone, J. Two-dimensional flexible nanoelectronics. *Nat. Commun.* **5**, 5678 (2014).

2. Mak, K. F. & Shan, J. Photonics and optoelectronics of 2D semiconductor transition metal dichalcogenides. *Nat. Photonics* **10**, 216–226 (2016).
3. Schaibley, J. R. et al. Valleytronics in 2D materials. *Nat. Rev. Mater.* **1**, 16055 (2016).
4. Xiao, D., Yao, W. & Niu, Q. Valley-contrasting physics in graphene: magnetic moment and topological transport. *Phys. Rev. Lett.* **99**, 236809 (2007).
5. Xu, X., Yao, W., Xiao, D. & Heinz, T. F. Spin and pseudospins in layered transition metal dichalcogenides. *Nat. Phys.* **10**, 343–350 (2014).
6. Xiao, D., Liu, G. B., Feng, W. X., Xu, X. D. & Yao, W. Coupled spin and valley physics in monolayers of MoS_2 and other group-VI dichalcogenides. *Phys. Rev. Lett.* **108**, 196802 (2012).
7. Mak, K. F., Xiao, D. & Shan, J. Light-valley interactions in 2D semiconductors. *Nat. Photonics* **12**, 451–460 (2018).
8. Cheng, J. et al. Chiral selection rules for multi-photon processes in two-dimensional honeycomb materials. *Opt. Lett.* **44**, 2141–2144 (2019).
9. Xiao, J. et al. Nonlinear optical selection rule based on valley-exciton locking in monolayer WS_2. *Light. Sci. Appl.* **4**, e366 (2015).
10. Mak, K. F., He, K., Shan, J. & Heinz, T. F. Control of valley polarization in monolayer MoS2 by optical helicity. *Nat. Nanotechnol.* **7**, 494 (2012).
11. He, K. et al. Tightly bound excitons in monolayer WSe_2. *Phys. Rev. Lett.* **113**, 026803 (2014).
12. Wang, G. et al. B. Giant enhancement of the optical second-harmonic emission of WSe_2 monolayers by laser excitation at exciton resonances. *Phys. Rev. Lett.* **114**, 097403 (2015).
13. Song, Z. et al. Tunable valley polarization and valley orbital magnetic moment Hall effect in honeycomb systems with broken inversion symmetry. *Sci. Rep.* **5**, 13906 (2015).
14. Lundt, N. et al. Optical valley Hall effect for highly valley-coherent exciton-polaritons in an atomically thin semiconductor. *Nat. Nanotechnol.* **14**, 770–775 (2019).
15. Jones, A. M. et al. Optical generation of excitonic valley coherence in monolayer WSe_2. *Nat. Nanotechnol.* **8**, 634–638 (2013).
16. Hao, K. et al. Direct measurement of exciton valley coherence in monolayer WSe_2. *Nat. Phys.* **12**, 677–682 (2016).
17. Neumann, A. et al. Opto-valleytronic imaging of atomically thin semiconductors. *Nat. Nanotechnol.* **12**, 329–334 (2017).
18. Luo, Y. K. et al. Opto-valleytronic spin injection in monolayer MoS_2/few-layer graphene hybrid spin valves. *Nano Lett.* **17**, 3877–3883 (2017).
19. Zyuzin, A. A. & Zyuzin, A. Y. U. Spin and valley waves in Dirac semimetals with population imbalance. *Phys. Rev. B* **100**, 121402(R) (2019).
20. Malard, L. M., Alencar, T. V., Barboza, A. P. M., Mak, K. F. & de Paula, A. M. Observation of intense second harmonic generation from MoS_2 atomic crystals. *Phys. Rev. B* **87**, 201401 (2013).
21. Kumar, N. et al. Second harmonic microscopy of monolayer MoS_2. *Phys. Rev. B* **87**, 161403 (2013).
22. Li, Y. L. et al. Probing symmetry properties of few-layer MoS_2 and hBN by optical second-harmonic generation. *Nano Lett.* **13**, 3329–3333 (2013).
23. Clark, D. J. et al. Strong optical nonlinearity of CVD-grown MoS_2 monolayer as probed by wavelength-dependent second-harmonic generation. *Phys. Rev. B* **90**, 121409 (2014).
24. Hsu, W. T. et al. Second harmonic generation from artificially stacked transition metal dichalcogenide twisted bilayers. *ACS Nano* **8**, 2951–2958 (2014).
25. David, S. N. et al. Rapid, all-optical crystal orientation imaging of two-dimensional transition metal dichalcogenide monolayers. *Appl. Phys. Lett.* **107**, 111902 (2015).
26. Psilodimitrakopoulos, S. et al. Ultrahigh-resolution nonlinear optical imaging of the armchair orientation in 2D transition metal dichalcogenides. *Light. Sci. Appl.* **7**, 18005 (2018).
27. Psilodimitrakopoulos, S. et al. Twist angle mapping in layered WS2 by polarization-resolved second harmonic generation. *Sci. Rep.* **7**, 14285 (2019).
28. Zhao, M. et al. Atomically phase-matched second-harmonic generation in a 2D crystal. *Light. Sci. Appl.* **5**, e16131 (2016).
29. Yin, X. et al. Edge nonlinear optics on a MoS_2 atomic monolayer. *Science* **344**, 488–490 (2014).
30. Karvonen, L. et al. Rapid visualization of grain boundaries in monolayer MoS2 by multiphoton microscopy. *Nat. Commun.* **8**, 15714 (2017).
31. Haussühl, S. *Physical Properties roof Crystals* (Wiley, Weinheim, 2007).
32. Hipolito, F. & Pereira, V. M. Second harmonic spectroscopy to optically detect valley polarization in 2D materials. *2D Mater.* **4**, 021027 [039501] (2017).
33. McIver, J. W., Hsieh, D., Steinberg, H., Jarillo-Herrero, P. & Gedik, N. Control over topological insulator photocurrents with light polarization. *Nat. Nanotechnol.* **7**, 96–100 (2011).
34. Golub, L. E. & Tarasenko, S. A. Valley polarization induced second harmonic generation in graphene. *Phys. Rev. B* **90**, 201402(R) (2014).
35. Wehling, T. O., Huber, A., Lichtenstein, A. I. & Katsnelson, M. I. Probing of valley polarization in graphene via optical second-harmonic generation. *Phys. Rev. B* **91**, 041404(R) (2015).
36. Wang, G. et al. Excitons in atomically thin transition metal dichalcogenides. *Rev. Mod. Phys.* **90**, 021001 (2018).
37. Li, T. & Galli, G. Electronic properties of MoS_2 nanoparticles. *J. Phys. Chem. C* **111**, 16192–16196 (2007).
38. Zhu, Z. Y., Cheng, Y. C. & Schwingenschlögl, U. Giant spin-orbit-induced spin splitting in two-dimensional transition-metal dichalcogenide semiconductors. *Phys. Rev. B* **84**, 153402 (2011).
39. Kormányos, A. et al. k·p theory for two-dimensional transition metal dichalcogenide semiconductors. *2D Mater.* **2**, 022001 (2015).
40. Ho, Y. W. et al. Measuring valley polarization in transition metal dichalcogenides with second-harmonic spectroscopy. *ACS Photonics* **7**, 925–931 (2020).
41. Goryca, M., Wilson, N. P., Dey1, P., Xu, X. & Crooker, S. A. Detection of thermodynamic "valley noise" in monolayer semiconductors: access to intrinsic valley relaxation time scales. *Sci. Adv.* **5**, eaau489 (2019).
42. Boyd, R. W. *Nonlinear Optics*. 3rd edn (Academic Press, San Diego, 2008).
43. Maragkakis, G. M. et al. Imaging the crystal orientation of 2D transition metal dichalcogenides using polarization-resolved second-harmonic generation. *Opto-Electron. Adv.* **2**, 190026 (2019).
44. Paradisanos, I. et al. Prominent room temperature valley polarization in WS2/graphene heterostructures grown by chemical vapor deposition. *Appl. Phys. Lett.* **116**, 203102 (2020).
45. Chou, C.-K. et al. Polarization ellipticity compensation in polarization second-harmonic generation microscopy without specimen rotation. *J. Biomed. Opt.* **13**, 014005 (2008).
46. Nayak, P. K. et al. Robust room temperature valley polarization in monolayer and bilayer WS_2. *Nanoscale* **8**, 6035–6042 (2016).
47. Zhu, B. et al. Anomalously robust valley polarization and valley coherence in bilayer WS_2. *Proc. Natl Acad. Sci. USA* **111**, 11606–11611 (2014).
48. Frisenda, R. et al. Recent progress in the assembly of nanodevices and van der Waals heterostructures by deterministic placement of 2D materials. *Chem. Soc. Rev.* **47**, 53–68 (2018).
49. Jayasena, B. & Melkote, S. N. An investigation of PDMS stamp assisted mechanical exfoliation of large area graphene. *Procedia Manuf.* **1**, 840–853 (2015).
50. Castellanos-Gomez, A. et al. Deterministic transfer of two-dimensional materials by all-dry viscoelastic stamping. *2D Mater.* **1**, 011002 (2014).

ACKNOWLEDGEMENTS

We would like to acknowledge financial support by the Hellenic Foundation for Research and Innovation (HFRI) under the "First Call for HFRI Research Projects to support Faculty members and Researchers and the procurement of high-cost research equipment grant" (Project No. HFRI-FM17-3034). This research has been co-financed by the European Union and Greek national funds through the Operational Program Competitiveness, Entrepreneurship and Innovation, under the call European R & T Cooperation-Grant Act of Hellenic Institutions that have successfully participated in Joint Calls for Proposals of European Networks ERA NETS (National project code: GRAPH-EYE T8EPA2-00009 and European code: 26632, FLAGERA). Support by the European Research Infrastructure NFFA-Europe, funded by the EC's H2020 framework program for research and innovation under grant agreement no. 654360, is also gratefully acknowledged.

AUTHOR CONTRIBUTIONS

L.M., S.P., E.S., and G. Kioseoglou planned the project; S.P., L.M., and G.M.M. designed the experiment; S.P., G.M.M., and I.D. conducted the optical experiments; L.M., S.P., and G.M.M. conducted the data analysis; A.L. provided technical support; L.M. elaborated the theoretical model; G. Kourmoulakis prepared the samples; E.S. and G. Kioseoglou guided the research. All authors contributed to the discussion and preparation of the manuscript.

COMPETING INTERESTS

The authors declare no competing interests.

ADDITIONAL INFORMATION

Supplementary information is available for this paper at https://doi.org/10.1038/s41699-020-00183-z.

Correspondence and requests for materials should be addressed to L.M. or E.S.

Reprints and permission information is available at http://www.nature.com/reprints